Desalination 603 (2025) 118679

Contents lists available at ScienceDirect

Desalination

journal homepage: www.elsevier.com/locate/desal

# Optimizing the integration of nickel hexacyanoferrate with hollow mesoporous carbon spheres (HMCSs) for highly efficient capacitive deionization

Shu Zhang [a], Zinan Ye [b], Mengyu Ma [a], Pengcheng Yin [a], Yang Bao [a], Feihu Li [a,b,*]

[a] Collaborative Innovation Center of Atmospheric Environment and Equipment Technology, Jiangsu Key Laboratory of Atmospheric Environment Monitoring and Pollution Control, School of Environmental Science and Engineering, Nanjing University of Information Science and Technology, 219 Ningliu Road, Nanjing 210044, China

[b] NUIST Reading Academy, Nanjing University of Information Science and Technology, 219 Ningliu Road, Nanjing 210044, China

## HIGHLIGHTS

- A "ship-in-the-boat" approach was used to prepare yolk-shell nanocomposites.
- The nanocomposites integrate a Prussian Blue Analog (PBA) with hollow mesoporous carbon spheres (HMCS).
- The resulting PBA@HMCS electrodes demonstrated exceptional CDI performance.
- The yolk-shell PBA@HMCS-3 electrode showed high cation repulsion of $K^+$.

## GRAPHICAL ABSTRACT

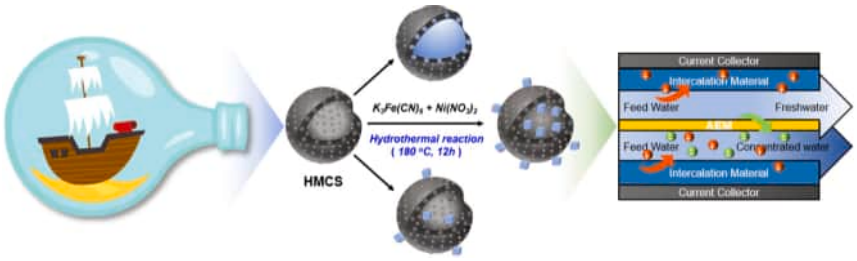


## ARTICLE INFO

*Keywords:*
Prussian blue analogue (PBA)
Hollow mesoporous carbon sphere (HMCS)
Electrosorption
Electrochemical water desalination
Selectivity

## ABSTRACT

Capacitive deionization (CDI) is a promising water desalination technology known for its energy efficiency and low environmental impact. Charge-transfer materials (e.g., Prussian blue analogues, PBAs) have gained much attention as electrodes for CDI due to their much higher salt adsorption capacities (SACs) beyond conventional carbon-based electrodes, though they face challenges such as conductivity, stability, and ion transfer kinetics. Integrating these charge-transfer materials with carbon offers a promising strategy to enhance CDI performance and address these limitations. Herein, using a stepwise "ship-in-the-boat" approach, we incorporated a typical PBA, i.e., NiHCF, with hollow mesoporous carbon spheres (HMCS) to yield hierarchical composite materials (i.e., PBA@HMCS). This composite combines the protective and conductive roles of carbon materials with the high ion storage capacity of PBAs. The resulting PBA@HMCS electrodes demonstrated exceptional CDI performance, with a maximum salt adsorption capacity of 80.5 mg $g^{-1}$ in 500 mg $L^{-1}$ NaCl solution at 1.2 V. Notably, the PBA@HMCS-1 electrode exhibited enhanced cycling stability, while the unwrapped PBA micropellets showed reduced performance. Furthermore, our investigation revealed the high affinity of PBA@HMCS electrodes for $Na^+$ over other ions in synthetic brine, and particularly, the yolk-shell PBA@HMCS-3 electrode demonstrated high repulsion to $K^+$, highlighting its potential for selectively extracting specific ions from dicationic brines with $K^+$ ions. This study highlights the potential of hierarchical yolk-shell PBA@HMCS as a promising CDI electrode

* Corresponding author at: Collaborative Innovation Center of Atmospheric Environment and Equipment Technology, Jiangsu Key Laboratory of Atmospheric Environment Monitoring and Pollution Control, School of Environmental Science and Engineering, Nanjing University of Information Science and Technology, 219 Ningliu Road, Nanjing 210044, China.
*E-mail address:* fhli@nuist.edu.cn (F. Li).

https://doi.org/10.1016/j.desal.2025.118679
Received 4 December 2024; Received in revised form 25 January 2025; Accepted 9 February 2025
Available online 10 February 2025

and underscores the need for continued exploration into the hierarchically structural design of composite materials for high-performance CDI platforms.

## 1. Introduction

With climate change and the explosive population growth globally, the consumption of water resources is increasing year by year, leading to a drastic shortage of freshwater resources around the world [1,2]. Since the oceans of our planet account for over 96 % of the Earth's water resources, the extraction of freshwater resources from seawater, i.e., seawater desalination, offers us a very promising solution to the shortage of freshwater resources [3]. Conventional desalination technologies including reverse osmosis (RO), electrodialysis (ED), multi-stage flash (MSF), and multi-effect desalination (MED) have been extensively studied and practically applied to engineering, but they also suffered from large capital expenditures, high energy consumption and operation costs, and corrosion or scaling [3–5]. Over the past several decades, capacitive deionization (CDI) has offered significant advantages in the desalination of low to medium-salinity water, showcasing impressive energy efficiency and cost-effectiveness [6,7]. As an emerging technology, CDI is now being extensively tested as a promising alternative for seawater desalination, wastewater remediation, and water softening on a laboratory scale [8]. CDI technology is usually operated inside a cell with a pair of electrodes coupled with a saline flow, or a mixture of saline and flow-electrode (termed as FCDI), both of which are based on electrosorption or Faradaic (charge transfer) reaction at the electrode/water interfaces [8,9].

It is well known that the electrode materials are crucial in determining the performance of CDI, and the design and fabrication of electrode materials with high salt adsorption capacity (SAC) and high salt adsorption rate (SAR) is therefore a vital and challenging task for maximizing and optimizing the CDI salination capacity [10–12]. Ideally, electrode materials suitable for CDI should possess a porous structure, high specific surface area, excellent electrical conductivity, good wettability, and chemical stability [13,14]. In terms of the above standards, carbon materials such as activated carbon (AC) [15], mesoporous carbon [16], carbon nanotubes (CNTs) [17], and graphene [18,19] were widely used as CDI electrodes. Despite significant advancements in these carbon materials-based CDI, the low SACs of such carbon electrodes ($<$ 20 mg $g^{-1}$) are one of the most challenging limitations hindering the practical application of CDI technology [20]. In this context, charge-transfer materials (also referred to as Faradaic or redox-active materials that undergo Faradaic reactions at the electrode/water interfaces) have emerged as a promising alternative, offering enhanced SACs and improved electrochemical performance that could effectively address these challenges [10,21,22].

As a classical Faradaic material, Prussian blue analogues (PBAs) have attracted much attention in the CDI community due to their low cost, high capacity, and structural tailorability [21,23]. PBAs are metal-organic frameworks with robust three-dimensional open structures that provide large ion channels, and thereof enable rapid transport and diffusion of a wide range of ions, and thus reversible storage of such ions inside these channels [23,24]. For instance, nickel hexacyanoferrate (NiHCF) has been shown a large spacing volume for the insertion of sodium ($Na^+$) and potassium ($K^+$) ions, good energy efficiency, excellent structural durability, and significantly long cycle life when used as electrodes for aqueous $Na^+$ and $K^+$ batteries [24]. While PBAs have demonstrated high desalination capacities in diverse platforms such as rocking-chair CDI (RCDI) [25] and membrane CDI (MCDI) [26], their low electrical conductivity presents a challenge that cannot be overlooked [23]. This reduced conductivity can limit the efficiency of ion transfer during the deionization process, potentially hindering the overall performance of CDI systems [27].

Despite this limitation, however, PBAs can still play a pivotal role in CDI applications when strategically integrated with conductive materials [28–34]. By combining PBAs with highly conductive carbon-based electrodes, we can create composite materials that capitalize on the high SACs of PBAs while mitigating conductivity issues. Following this strategy, conductive materials such as reduced graphene oxide (rGO) [28], reduced graphene oxide aerogel (rGA) [29], three-dimensional (3D) carbon nanosheet networks (3 DC) [30], carbon cloth [31], metal-organic framework (MOF)-derived carbon [33], hollow graphite tube (HGT) [34], CNTs [35], and MXene [36] have been successfully incorporated with PBAs to form novel composite electrodes, demonstrating enhanced CDI performance compared to systems without such conductors. To leverage the synergy between PBAs and the conductive components, one promising approach is the hierarchically structural design of the resulting PBAs/carbon composites. The hierarchical structures offer higher surface areas, additional ion transport pathways and thereof more efficient desalination performance [35,37]. In particular, the design of hierarchically yolk-shell structured composites with carbon as the shell and charge-transfer materials as the core has been shown excellent structural durability and cycling stability when applied in CDI [20,38]. The unique yolk-shell structured materials not only display fast ion diffusion across the solid-cavity-solid interface but also provide a tailorable cavity for ion storage, leading to better CDI performance than their core-shell counterparts [20]. However, the yolk-shell design of PBAs/carbon composites for CDI has yet to be explored although there are several successful examples of embedding carbon [39], phosphate [20] and layered double oxides [40] into hollow mesoporous carbon spheres (HMCS) by layer-by-layer coating or one-pot solvothermal approaches. The primary challenge in producing such a yolk-shell structured PBA@HMCS is the relatively lower thermostability of PBAs (usually $<$180 °C) [41], which will finally turn into metal carbides in the formation of carbon shells particularly by carbonization. The tailorability of pore sizes over the HMCS shells, however, offers a feasible option of preparing yolk-shell PBA@HMCS by diffusive introducing PBA precursor into the HMCS cavities followed by the formation of PBAs via a nanospace-confined growth approach [20,42]. Therefore, a comprehensive nanospace-confined growth of PBAs within HMCS of tailorable pores (“ship-in-the-bottle”) is necessary for optimizing the integration of PBAs with HMCS to leverage the synergy of both components for high-performance CDI.

Here, we present the synthesis of yolk-shell NiHCF-embedded HMCS composites (denoted as PBA@HMCS) via a “ship-in-the-bottle” approach and demonstrate their desalination performance in a symmetric RCDI platform experimentally. The HMCS is synthesized using a stepwise condensation-calcination-etching approach. The mesoporous channel sizes of the HMCS shell which acts as ion diffusion pathways, are tailored by changing its precursor composition, enabling highly efficient diffusive introduction of NiHCF precursors into the HMCS vacancies and thereby the formation of yolk-shell PBA@HMCS upon properly hydrothermal treatment. Electrochemical analyses are performed to evaluate their electrochemical properties in a three-electrode system. These PBA@HMCS composites are then integrated into an RCDI cell, enabling high performance CDI applications with specific ion repulsion against $K^+$ ions. Therefore, our study presents a group of unique and rationally designed yolk-shell PBA@HMCS composites for highly-performance CDI desalination and highlights the need for more hierarchically structural designs of composite electrodes for the separation of value-added elements via CDI systems.

## 2. Experimental section

All chemicals are of analytical grade or above and used as received.

Ultrapure deionized water (DI $H_2O$, 18.2 MΩ·cm at 25 °C) was used for preparing all solutions in this study.

### 2.1. Preparation and characterization of PBA@HMCS

Hollow mesoporous carbon spheres (HMCSs) with tunable pore sizes were first synthesized following the protocol reported elsewhere [43]. In brief, a mixture (12 mmol) of tetrapropyl orthosilicate (TPOS, 97 %, Aladdin Chemical Co.) and tetraethyl orthosilicate (TEOS, Sinopharm Chemical Co.) (TPOS:TEOS molar ratio = 0.75) was added into a mixed solution of ethanol (EtOH, 70 mL), DI $H_2O$ (10 mL), and ammonium hydroxide (3 mL, 25–28 %, Aladdin Chemical Co.), and then the resulting solution was stirred at room temperature for 15 min. Subsequently, resorcinol (0.4 g, 99 %, Macklin Inc.) and formaldehyde (0.56 mL, 37–40 %, Sinopharm Chemical Co.) were added to the above solution and stirred for 24 h to allow the condensation of resorcinol formaldehyde (RF) over the surface of $SiO_2$ nanospheres. The precipitate was separated from the suspension by centrifugation, rinsed with excess DI $H_2O$ and EtOH, followed by drying at 60 °C overnight. Then the resulting precipitate (i.e., $SiO_2$@$SiO_2$/RF) was pyrolyzed at 700 °C for 5 h under a $N_2$ atmosphere to obtain $SiO_2$@$SiO_2$/C nanospheres, which was further rinsed and etched with sodium hydroxide (NaOH, 4 M) to remove its silicon dioxide component, yielding the hollow mesoporous carbon spheres denoted as HMCS-1. Using the same protocol with TPOS: TEOS molar ratios of 0.5 and 0, HMCS-2 and HMCS-3 were obtained respectively (Scheme 1).

A simple hydrothermal method (the alleged "ship-in-the-bottle" method) was employed to integrate the Prussian blue analogue (PBA, as the 'ship') with HMCS (as the 'bottle'). Typically, an aqueous solution (15 mL) containing 0.02 M potassium ferricyanide ($K_3Fe(CN)_6 \geq 99.5$ %, Sinopharm Chemical Co.) and HMCSs (100 mg) has been vigorously stirred for 24 h, followed by mixing with 15 mL of 0.04 M nickel nitrate hexahydrate ($Ni(NO_3)_2{\cdot}6H_2O$, ≥ 99 %, Sinopharm Chemical Co.) and then sonicating for 10 min. Subsequently, the black solution was transferred into a 60 mL Teflon-lined stainless-steel autoclave, and heated in an oven at 180 °C for 12 h. After cooling down to room temperature, the synthetic black pellet was collected by centrifugation, rinsed with excess DI $H_2O$ and EtOH, followed by drying at 60 °C overnight. In terms of the HMCS, the synthetic nanocomposites were denoted by PBA@HMCS-1, PBA@HMCS-2, and PBA@HMCS-3, respectively, and stored in a glass desiccator for further use.

The crystal phases of all samples were analyzed by X-ray diffraction (XRD) using a Shimadzu XRD-6100 X-ray diffractometer with Cu-Kα radiation at a tube voltage of 40 kV and a tube current of 30 mA. Surface elements were examined by X-ray fluorescence spectroscopy (XRF) using a handheld DELTA DC-4000 XRF analyzer (Olympus, USA) with soil mode (3-beam). The microscopic morphology was recorded on a Hitachi SU1510 scanning electron microscope (SEM) and a Philips TECNAI 12 transmission electron microscope (TEM), respectively. Fourier transform infrared (FTIR) spectroscopy was performed on a Nicolet iS5 infrared spectrometer (Thermo Fisher, USA) using the KBr pellet method. X-ray photoelectron spectroscopic (XPS) data were obtained with an electron spectrometer (UIVAC-PHI, Japan) using 300 W Al Kα radiation, with the adventitious carbon species C 1 s (284.8 eV) for binding energy (BE) correction.

### 2.2. Electrochemical measurements

All electrochemical measurements were carried out in 1.0 M NaCl solution with a three-electrode system (platinum foil as counter electrode, Ag/AgCl as reference electrode, and PBA@HMCS as working electrode) on a CS310H electrochemical workstation (Correst Instruments Inc., China) at ambient temperature. The working electrodes were prepared by combining PBA@HMCS, acetylene black (Alfa Aesar, Shanghai, China), and polyvinylidene fluoride (PVDF, Aladdin Chemical Co.) in a mass ratio of 8:1:1. The mixture was then dispersed and ground in an agate mortar using 1-methyl-2-pyrrolidone as dispersant until a homogeneous slurry was obtained. The slurry was sequentially applied onto a clean graphite paper (1 cm × 1 cm), which was dried in a vacuum at 80 °C for 2 h, and then used as the working electrode. Cyclic voltammetry (CV) was performed at a scan rate of 5–100 mV $s^{-1}$. Galvanostatic charge-discharge (GCD) analysis was conducted at a current density of 0.3–5 A $g^{-1}$. Electrochemical impedance spectroscopy (EIS) measurement was examined at a frequency of $10^5$–0.01 Hz, and the applied bias voltage and ac amplitude were set at open-circuit potential and 5 mV, respectively. The specific gravimetric capacitance of the electrode was calculated by Eq. (1),

$$C_m = \frac{I \times \Delta t}{m \times \Delta V} \quad (1)$$

where $\boldsymbol{C}_m$ is the specific capacitance determined by GCD discharge curves (F $g^{-1}$), $m$ stands for the mass of the active materials in the electrode (g), $\boldsymbol{I}$ represents the discharge current (A), $\boldsymbol{\Delta t}$ is the discharge time (s), and $\boldsymbol{\Delta V}$ represents the potential window of the discharge (V).

### 2.3. Capacitive deionization experiments

Following the same protocol described earlier [12], the electrodes (30 mg in mass, ~ 30 μm in thickness, 8:1:1 of PBA:acetylene black: PVDF) for CDI tests were prepared on a 5 cm × 5 cm clean carbon paper and then assembled into an RCDI cell (Fig. S1a, Supplementary data). The RCDI platform is composed of an RCDI cell with two chambers (2.5 mL each) separated by the AEM membrane, an electrochemical workstation equipped with a benchtop PC, two peristaltic pumps, and a conductivity meter (Fig. S1b). The CDI tests were performed in batch mode under constant voltage conditions [25] with a total volume of feed

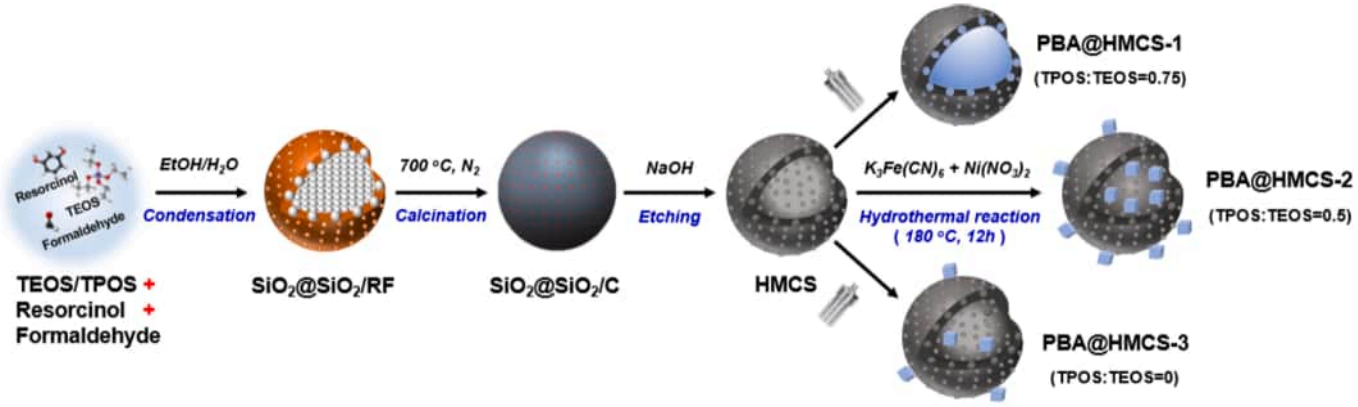


**Scheme 1.** Schematic illustration of the preparation of PBA@HMCS nanocomposites via the "ship-in-the-boat" approach.

solution of 30 mL (Fig. S1c). By convention, voltages of 0.6–1.2 V and feed solutions of 100–500 ppm NaCl solutions were used to examine the effects of cell voltage and feed solution concentration on the CDI performance, respectively. The salt adsorption capacity of the electrode was determined using Eq. (2),

$$SAC = \frac{(C_0 - C_e)V}{m} \tag{2}$$

where $C_0$ and $C_e$ stand for the initial and the final concentration of the feed solution (mg·L$^{-1}$), respectively, $V$ is the solution volume (mL), and $m$ refers to the mass of the active electrode material on one side (g).

The charge efficiency ($\Lambda$, %) was calculated according to Eq. (3),

$$\Lambda = \frac{SAC \times F}{M \times \Sigma} \tag{3}$$

where $F$ is the Faraday constant (96,485C mol$^{-1}$), $\Sigma$ refers to the total charge associated with the integrated corresponding current (C g$^{-1}$), and $M$ (in g mol$^{-1}$) stands for the molar weight of the target salt in the feed brine.

### 2.4. Selective adsorption of ions

To evaluate the ion-selective property of PBA@HMCS electrodes toward specific ions, a solution (40 mL) with $Li^+$:$Na^+$:$K^+$:$Mg^{2+}$:$Ca^{2+}$ = 4:79:16:18:5 (molar ratio) was prepared using the same ratio in the real brine from the East Taijinaier Salt Lake and further used as the synthetic brine for the selectivity evaluation following the same procedure in our earlier work [11]. Saline samples were collected every five minutes (i.e., 5 charge/discharge cycles) and the concentrations of different ions were measured using an Optima 8000 inductively coupled plasma atomic emission spectrometer (ICP-OES, PerkinElmer, USA). The selectivity of monovalent ions over divalent ions is quantified by a separation factor ($\beta_{M/D}$), which was determined by Eq. (4),

$$\beta_{M/N} = \left(\frac{C_{M,initial} - C_{M,final}}{C_{N,initial} - C_{N,final}}\right)\left(\frac{C_{N,initial}}{C_{M,initial}}\right) \tag{4}$$

where M and N represent $M^{x+}$ and $N^{y+}$ ions, respectively, and $C_{M,\ initial}$, $C_{M,\ final}$, $C_{N,\ initial}$ and $C_{N,\ final}$ are the concentrations of these ions at the beginning and the end of the interpolated half cycle, respectively.

## 3. Results and discussions

### 3.1. Characterizations of as-prepared PBA@HMCS

The crystal structure of as-prepared PBA@HMCS nanocomposites was verified by XRD to belong to the cubic F-43$m$ (216) group with a lattice parameter of 10.23 Å, in good agreement with our earlier observation [12]. The yellow shaded peaks in Fig. 1a match well with the standard JCPDS # 86–0501 card of nickel iron cyanide hydrate (Ni[Fe(CN)$_6$]$_{0.667}$(H$_2$O)$_{0.333}$), indicative of successful preparation of PBAs. The XRD pattern of HMCS-1 is characterized by two broad, diffuse humps at 2θ of 15–30° and 40–50° (Fig. S2a), indicating its amorphous nature. In contrast, the reflections of (220), (420), and (440) in NiHCF exhibit splitting into two equal branches (Fig. S2b), a consequence of lattice expansion caused by the intrinsic alkali metals [44]. Upon hydrothermal integration with HMCS, the resulting PBA@HMCS nanocomposite displays a shift of all sharp peaks to higher 2θ regions, suggesting a decrease in interplanar spacing ($d$-spacing). This compression of the NiHCF crystal lattice is expected under the high-pressure conditions generated by the hydrothermal treatment (180 °C,

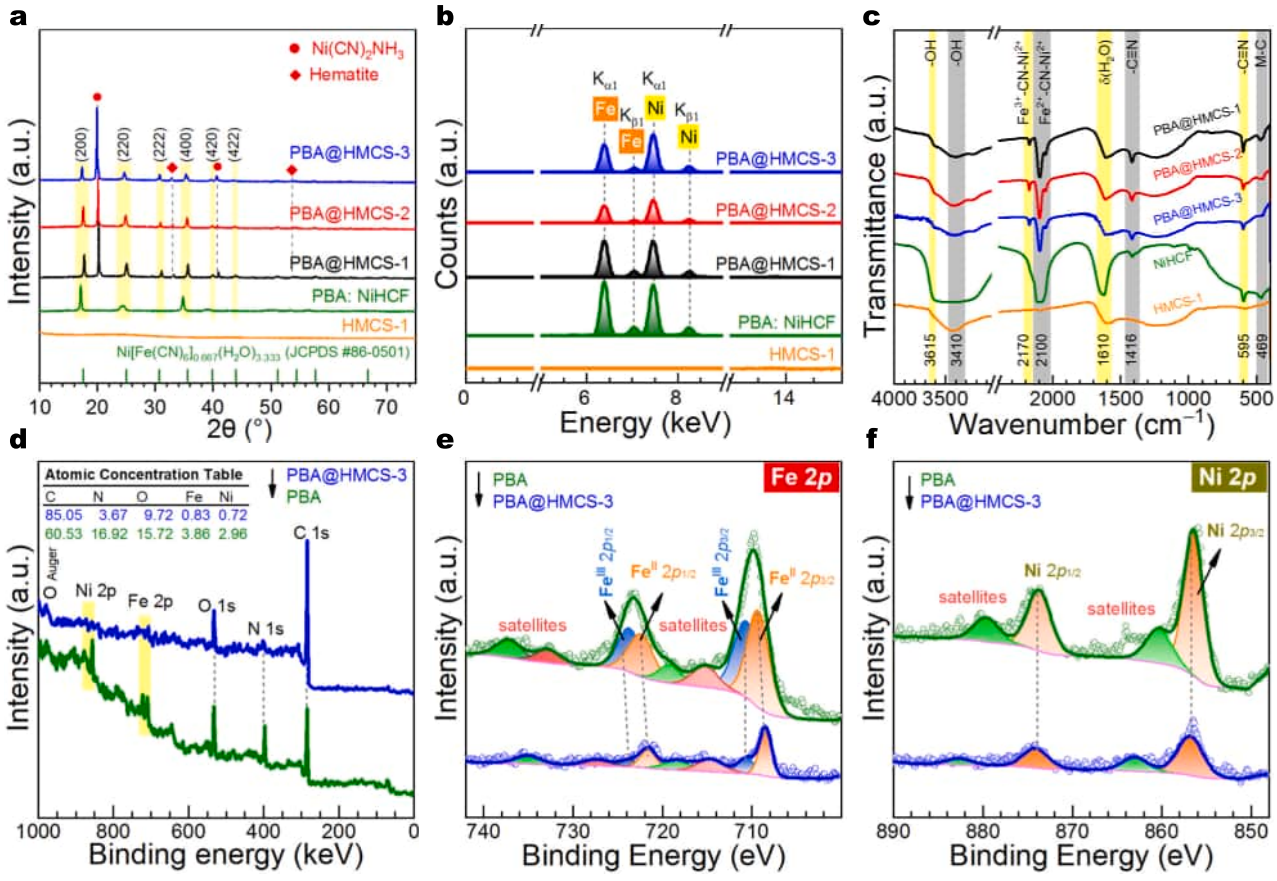


**Fig. 1.** (**a**) XRD patterns (note: the circle and diamond refer to ammonia nickel cyanide (JCPDS #74–1079) and hematite (JCPDS #89–0596), respectively), (**b**) XRF and (**c**) FTIR spectra of PBA@HMCS, PBA (i.e., NiHCF), and HMCS-1; (**d**) survey, (**e**) Fe 2p and (**f**) Ni 2p region XPS of PBA and PBA@HMCS-3.

12 h). Crystal size calculations using the Scherrer equation and the data of (200) reflection reveal a progressive increase in size from NiHCF (33.3 nm) to PBA@HMCS-1 (38.9 nm), PBA@HMCS-2 (40.2 nm), and PBA@HMCS-3 (41.7 nm). Notably, the hydrothermal process also led to the formation of new phases, including ammonia nickel cyanide (JCPDS #74–1079) and hematite (JCPDS #89–0596), which were not present in the original materials. It is believed that ammonia can be generated from the decomposition of nitrate ions in the presence of iron [45], thereby facilitating its coordination with nickel(II) cyanide complexes to form ammonia nickel cyanide mineral as byproducts from the complex reactions of $Ni(NO_3)_2$ and $K_3[Fe(CN)_6]$ under hydrothermal conditions. XRF spectra confirm the major detectable heavy elements of the as-prepared PBA@HMCS nanocomposites are iron and nickel, respectively (Fig. 1b), in good accordance with the above XRD results.

FTIR spectra shown in Fig. 1c indicate the presence of structural (3200 and 3615 $cm^{-1}$) and adsorbed water molecules (1610 $cm^{-1}$) [12], respectively within these samples. Besides, note that bands at 2170, 2100, and 2094 $cm^{-1}$ assignable to vibrations of −CN ($Fe^{3+}$), −CN ($Fe^{2+}$), and − C ≡ N− bond of cyanide-coordinated $Fe^{2+}$ and $Ni^{2+}$ [46,47], are also observed in all PBA@HMCS nanocomposites, and their spectra are comparable to that of the NiHCF (the olive curve), confirming the successful integrating of NiHCF with HMCS. The IR bands at 1416 and 595 $cm^{-1}$, and 464 $cm^{-1}$ correspond to the characteristic stretching of −C ≡ N− and M − C [12,46], respectively. Additionally, the survey XPS spectra of PBA and PBA@HMCS-3 reveal the presence of major elements in both samples, with much higher atomic concentration of carbon within PBA@HMCS-3 as expected (Fig. 1d). Note that a discontinuous feature was observed in the survey XPS spectrum of PBA@HCMS-3, which is likely to be derived from the surface inhomogeneities of HMCS particles, leading to uneven photoemission during the XPS characterization. A similar phenomenon has also been documented in other HMCS or hierarchical carbon samples [48,49]. Regional XPS like Fe 2p and Ni 2p verify that iron in both the PBA and the PBA@HMCS-3 is in +2 and +3 oxidation states while nickel is in +2 states (Fig. 1e–f).

TEM images confirm the hollow structure of all as-prepared HMCSs with approximate monodispersity (Fig. 2a–c). Their sizes range from 240 to 380 nm with mean diameters of approximately 280 to 320 nm, in good agreement with those reported elsewhere [43]. Notably, the shell of HMCS-1 with a TPOS/TEOS ratio of 0.75 is featured by many distinct and spokewise channels (highlighted by yellow arrows in Figs. 2a and S3a), which serve as the entrances for the precursors of PBAs, namely Ni $(NO_3)_2$ and $K_3[Fe(CN)_6]$. The size of these mesoporous channels can be precisely controlled by adjusting the TPOS/TEOS ratio in the synthetic mixture, with smaller channels resulting from a lower TPOS/TEOS ratio [43]. TEM images of PBA@HMCS confirm that PBA@HMCS-1 exhibits a mixture of yolk-shell and core-shell structure, where the hollow cores are mostly or entirely occupied by PBA crystals (Fig. 2d). In contrast, only a limited portion of the HMCS is filled with PBA in the cases of PBA@HMCS-2 and PBA@HMCS-3 (Fig. 2e–f). This difference in PBA loading can be attributed to the mesoporous channel size of the HMCS, which decreases in the order HMCS-1 > HMCS-2 > HMCS-3. SEM images of PBA@HMCS nanocomposites show that PBA@HMCS-1, PBA@HMCS-2, and PBA@HMCS-3 are aggregated together to form irregular bulks with diameters on the order of 50 μm (Fig. S3b-d). Images at higher magnification (Fig. S3c) indicate the presence of numerous nanosized PBA@HMCS particulates, consistent with the above TEM images. The $N_2$ absorption-desorption isotherms of HMCS-3 and PBA@HMCS-3 are classified as type II isotherms (IUPAC classification) with a type H3 hysteresis loop (Fig. S4a), indicating of the presence of mesopores due to the nonrigid aggregation of carbon nanoparticles [50]. This observation aligns with the TEM results presented earlier (Fig. 2). The Brunauer-Emmett-Teller (BET) surface areas of HMCS-3 and PBA@HMCS-3 are 770 and 616 $m^2\ g^{-1}$, respectively (Fig. S4a). Additionally, the pore size distribution derived from the desorption data using the Barrett-Joyner-Halenda (BJH) method further confirms the mesoporous structure of both samples (Fig. S4b).

### 3.2. Electrochemical properties of PBA@HMCS electrodes

The electrochemical properties of PBA@HMCS electrodes were evaluated by CV, GCD, and EIS with a three-electrode system in 1 M NaCl solution. Fig. 3a compares the CV curves of PBA@HMCS electrodes at a scan rate of 5 mV $S^{-1}$. Generally, a CV curve of rectangular shape typically reflects pure electric double layer (EDL) capacitance, while a quasi-rectangular or peak-shaped CV curve indicates the involvement of pseudocapacitance, CV curves of a mixed shape imply a mixed capacitance behavior [51,52]. The shape of all the CV curves indicates a clear synergistic effect of the EDL capacitance and pseudo-capacitance behavior, which are derived from the carbon constituent (i.e., HMCS) and PBA, respectively. A comparison of the CV curves of PBA, HMCS-3 and PBA@HMCS-3 further confirms the synergy between PBA and the HMCS components (Fig. S5a). A pair of well-defined redox peaks can be observed for all the CV curves of these composites over the potential

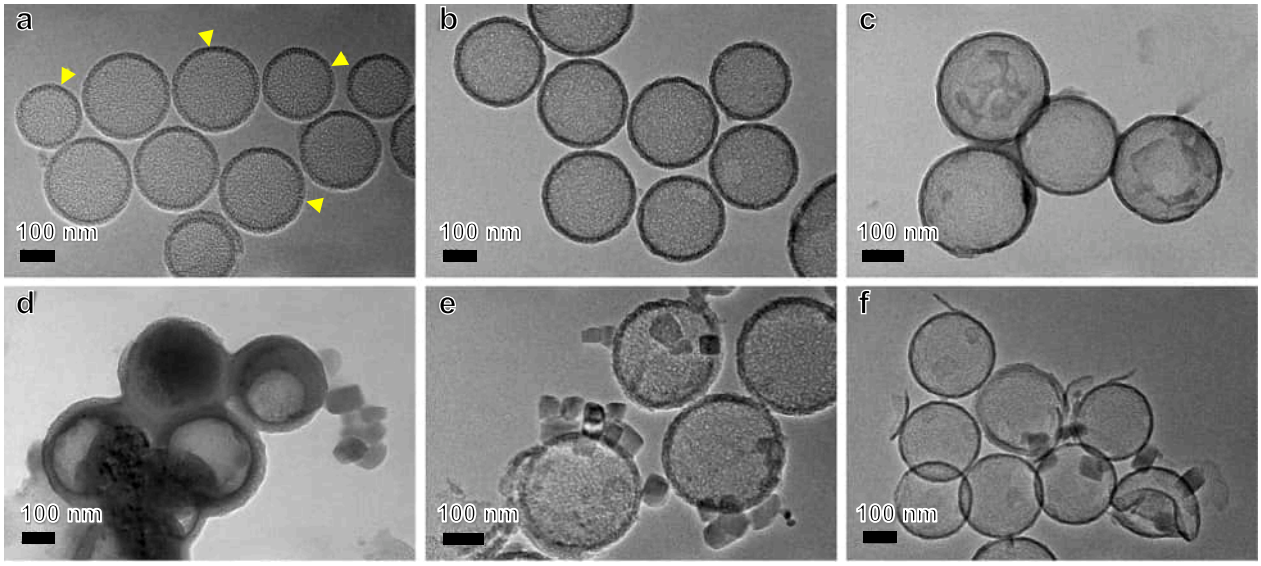


**Fig. 2.** TEM images of (**a**) HMCS-1, (**b**) HMCS-2, (**c**) HMCS-3, (**d**) PBA@HMCS-1, (**e**) PBA@HMCS-2, and (**f**) PBA@HMCS-3.

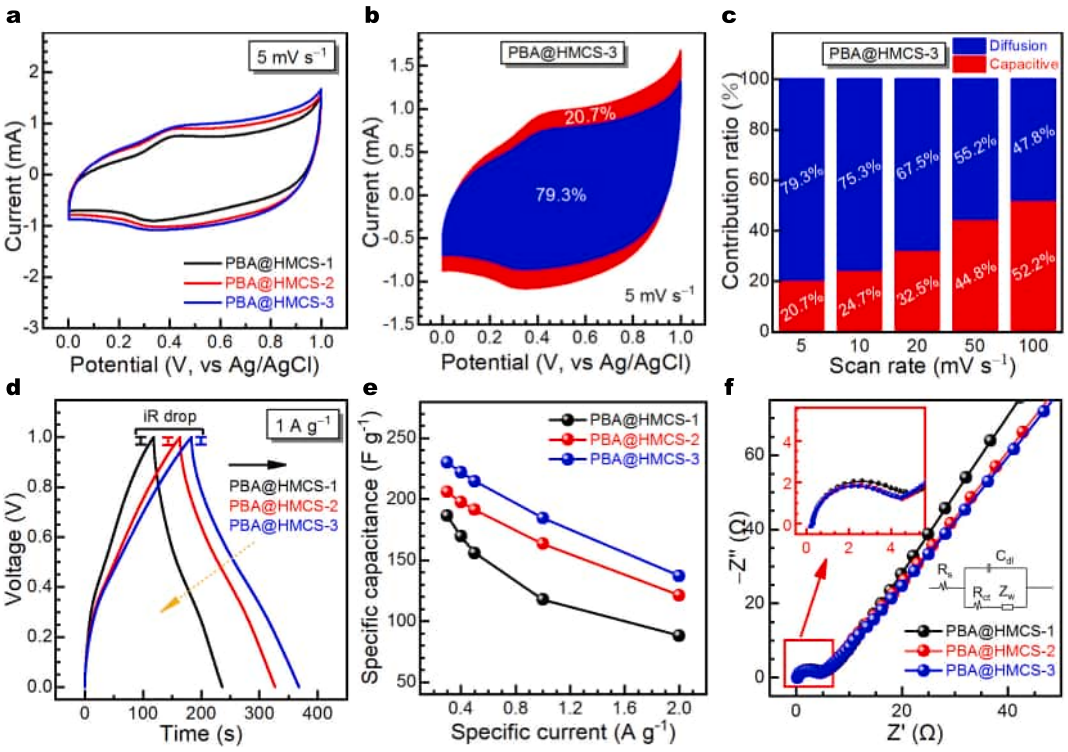


**Fig. 3.** Electrochemical characterizations of all PBA@HMCS electrodes in 1 M NaCl solution: (**a**) CV curves at 5 mV $s^{-1}$; (**b**) Capacitive- and diffusion-controlled contribution to the charge storage of PBA@HMCS-3 at 5 mV $s^{-1}$; (**c**) Contribution ratios of capacitive- and diffusion-controlled capacity for PBA@HMCS-3 at different scan rates; (**d**) GCD curves at 1 A $g^{-1}$; (**e**) Specific capacitances at different specific currents; and (**f**) Nyquist plots of EIS and the fitting curves, inset on the right is the equivalent circuit.

range of 0–1.0 V (Figs. 3a and S6), indicating a reversible redox reaction between $Fe^{II}$ and $Fe^{III}$ within NiHCF during the insertion and desertion of $Na^+$ [10]. The cathodic peak (at ~1 mA over the potential range of 0.3–0.5 V) represents the reduction of $Fe^{III}$ to $Fe^{II}$ owing to the desertion of $Na^+$ from NiHCF ($Na_2NiFe^{II}(CN)_6 \rightarrow Na^+ + e^- + NaNiFe^{III}(CN)_6$), while the anodic peak (at ~ −1 mA over 0.2–0.4 V) corresponds to the reverse process where $Fe^{II}$ is oxidized back to $Fe^{III}$ due to the insertion of $Na^+$ into the NiHCF ($NaNiFe^{III}(CN)_6 + e^- + Na^+ \rightarrow Na_2NiFe^{II}(CN)_6$) [24,53]. Note that the integral area of the CV curves of PBA@HMCS-3 is the largest among all the PBA@HMCS electrodes, indicating it has the highest specific capacitance and thus excellent desalination performance [30].

To further understand the capacitive and ion diffusion behaviors of the PBA@HMCS electrodes, we used the voltammetric sweep rate dependence (Fig. S6) and calculated the non-diffusion- (capacitive) and diffusion-controlled contribution according to Eq. (5) proposed by Dunn et al. [54],

$$i(V) = k_1 v + k_2 v^{1/2} \quad (5)$$

where $i(V)$ is the current response at a fixed potential $V$, $v$ is the scan rate (mV $s^{-1}$), $k_1$ and $k_2$ are adjustable parameters, $k_1 v$ and $k_2 v^{1/2}$ refer to the capacitive-controlled (non-diffusion) and the diffusion-controlled insertion, respectively. Taking the PBA@HMCS-3 as an example, the total charge storage contributions from diffusion and capacitive to the current response at a scan rate of 5 mV $s^{-1}$ are 79.3 % and 20.7 %, respectively (Fig. 3b). With the increase of the scan rate from 5 to 100 mV $s^{-1}$, the capacitive contribution increases from 20.7 % to 52.2 % in PBA@HMCS-3 (Fig. 3c), suggesting that its excellent electrochemical performance (i.e., charge storage and transfer) was realized by the good charge transport properties and fast ion diffusion ability [55]. Similar trends were also observed for other PBA@HMCS electrodes (Figs. S7-S9) with enhanced capacitive contributions at higher scan rates, which is attributed to the limited time for $Na^+$ ions to diffuse or insert into the electrodes [56].

Fig. 3d compares the GCD curves of the PBA@HMCS electrodes at a specific current of 1 A $g^{-1}$. All the PBA@HMCS electrodes exhibit a nonlinear distortion toward the upper right in the discharge curves (marked with a dash-line arrow) over the voltage range of 0.3–0.6 V (Fig. S10a–c), which corresponds to the redox behavior in the CV curves and demonstrates a Faradaic charge storage mechanism of these PBA electrodes [12]. A comparison of GCD curves of PBA, HMCS-3 and PBA@HMCS-3 shown in Fig. S5b also validates the same mechanism, particularly in the pristine PBA electrode. Moreover, at lower specific currents, more active sites are populated to transfer the resistance, thereby extending the duration of the charging and discharging plateaus. The PBA@HMCS-3 electrode has a longer plateau compared to PBA@HMCS-1 and PBA@HMCS-2, indicating that PBA@HMCS-3 is likely to show a higher specific capacitance and excellent electrochemical performance, consistent with the above CV results. The specific capacitances of PBA@HMCS composites at varying specific currents, calculated from the GCD discharge curve by using Eq. 1 [57], are depicted in Fig. 3e. With increasing specific current from 0.3 to 2.0 A $g^{-1}$, the specific capacitances of all the PBA@HMCS decrease accordingly. For instance, the specific capacitance of PBA@HMCS-3 at 0.3 A $g^{-1}$ is 230 F $g^{-1}$, much higher than those of PBA@HMCS-1 and PBA@HMCS-2 (186.4 and 206.0 F $g^{-1}$, respectively), suggesting a greater ion storage capacity and thereby an increased desalination capacity when utilized in CDI [12,23]. The high specific capacitance of PBA@HMCS-3 was believed to be attributed to the effective combination between HMCS and NiHCF particles, where the HMCS acted as a conductive bridge and provided ion and electron transport with a favorable conductive network structure, facilitating the ion transport and thus resulting to higher specific capacitance [58]. Consequently, it is plausible to forecast that the PBA@HMCS-3 electrode with the highest specific capacitance, may demonstrate superior desalination performance compared to the other electrodes. In addition, PBA@HMCS-3 also

demonstrates the smallest IR drops at specific currents <2.0 A $g^{-1}$ (Fig. S10d), indicating that the PBA@HMCS-3 electrode has the best CDI performance with the lowest charge transfer resistance at lower specific currents.

The Nyquist plots of all PBA@HMCS electrodes reveal that all electrodes exhibited a small semicircle in the high-frequency region and a steeply inclined straight line in the low and medium-frequency regions (Fig. 3f). The semicircle diameter represents the charge-transfer resistance ($\boldsymbol{R}_{ct}$) attributed to the Electric Double Layer (EDL) in parallel with the electric $\boldsymbol{R}_{ct}$ at the interface between the electrode and the electrolyte. By fitting experimental data with the equivalent circuit model (inset of Fig. 3f), the $\boldsymbol{R}_{ct}$ is determined to be 3.08, 2.82, and 2.69 Ω for PBA@HMCS-1, PBA@HMCS-2 and PBA@HMCS-3, respectively. The lowest $\boldsymbol{R}_{ct}$ of the PBA@HMCS-3 electrode indicates that it appears to show the best electron transfer ability among all these PBA@HMCS electrodes [36]. In addition, the Warburg impedance ($Z_w$) values derived from the diagonal line portions in the intermediate- and low-frequency regions decrease apparently in the order PBA@HMCS-1 > PBA@HMCS-2 > PBA@HMCS-3, implying PBA@HMCS-3 displays the most rapid interfacial ion migration rate, followed by other electrodes in reverse order [59]. This is in good agreement with the above CV and GCD results and can be explained by the fact that the best electrochemical performance of PBA@HMCS-3 is likely attributed to the synergistic effect of HMCS and NiHCF. The HMCS with high electrical conductivity not only serves as a backbone for the uniform growth of NiHCF to expose more electrochemical reactive active sites but also acts as a conductive bridge for charge transport through NiHCF.

### 3.3. Capacitive deionization performance

Following the same protocol specified elsewhere [12], the desalination performance of PBA@HMCS electrodes was initially examined in a one-sided RCDI cell with 100 mg $L^{-1}$ NaCl solution at 1.2 V in the constant-voltage mode (Fig. 4a). Typically, the curves of conductivity versus time exhibit distinct two phases — the charging phase when $Na^+$ insertion occurred (yellow-shaded region) followed by the discharging phase when $Na^+$ desertion happened (cyan-shaded region) over one desalination-regeneration cycle [6,28,60]. Compared to the other two electrodes, the PBA@HMCS-3 electrode showed a considerably faster rate and greater ability to capture $Na^+$ during the charging phase, in good agreement with the expectations from the above CV and GCD results (Fig. 3a, d, e). Quantitative calculations using Eq. 2 showed that the SAC of the PBA@HMCS-3 electrode in 100 mg $L^{-1}$ NaCl solution at 1.2 V was as high as 44.5 mg $g^{-1}$ (Fig. 4b), much greater than those of other PBA@HMCS electrodes (i.e., 11.7 and 27.1 mg $g^{-1}$ for PBA@HMCS-1 and PBA@HMCS-2, respectively). Note that the PBA@HMCS-1 electrode showed a relatively low SAC of 11.7 mg $g^{-1}$ with salt uptake of 34.3 %, far below other NiHCF coated by carbon (e.g., NiHCF@C) under the same conditions [12]. This disparity in desalination performance can be attributed to the unique structural configuration of PBA@HMCS-1 that was encapsulated closely by the HMCS shell with microporous channels (Fig. 2a, d), hindering the diffusion and transport of $Na^+$ and $Cl^-$ ions across the shell. As a consequence, the PBA@HMCS-1 is undersaturated, while the PBA@HMCS-3 is fully saturated during the CDI charging operation (Fig. 4a). Moreover, the Kim-Yoon plots (i.e., the SAR versus SAC profile, Fig. 4c) also indicate that the distance between the SAR versus SAC profiles and the upper-right corner of the panel

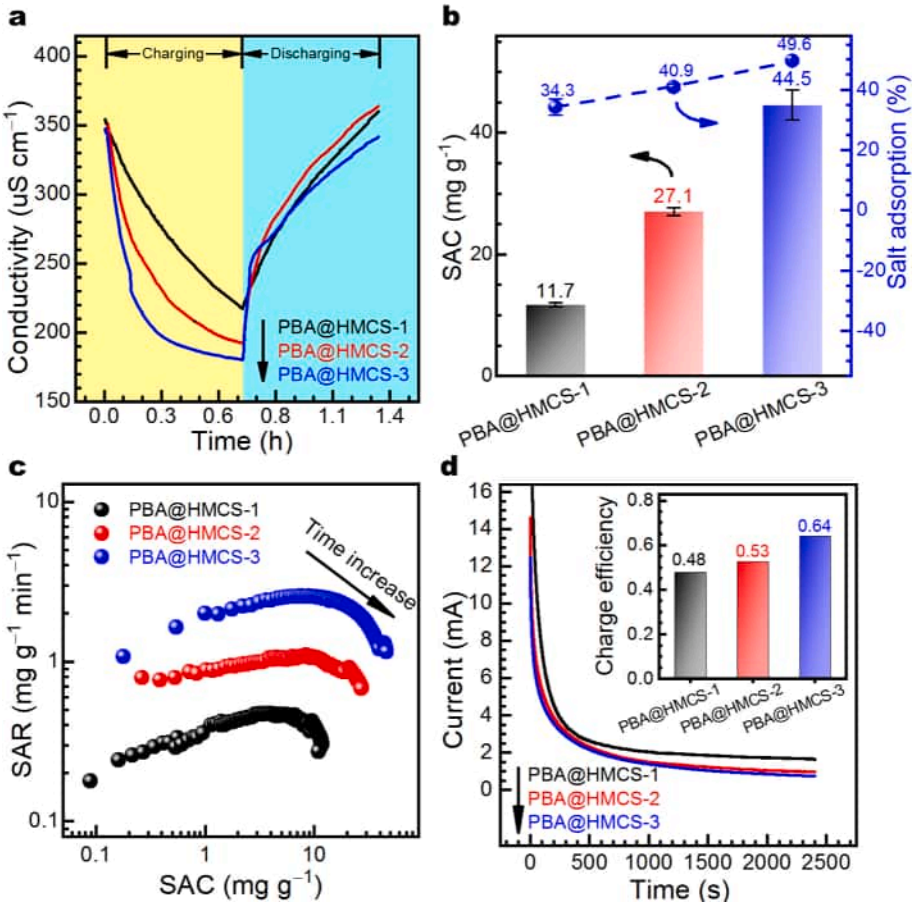


**Fig. 4.** (**a**) Plot of conductivity versus time in the 3rd run of RCDI operation of PBA@HMCS electrodes in 100 mg $L^{-1}$ NaCl solution at 1.2 V; (**b**) Salt adsorption capacity and the salt adsorption percentage of these PBA@HMCS electrodes; (**c**) Kim-Yoon plot; (**d**) Current responses and the corresponding charge efficiency.

decreases in the order PBA@HMCS-1 > PBA@HMCS-2 > PBA@HMCS-3, suggesting that the PBA@HMCS-3 electrode demonstrated a quite faster rate (SAR) and much greater capacity (SAC) for capturing $Na^+$ over its two counterparts in the same timescales [61]. Furthermore, the charging efficiencies at 1.2 V were calculated to be 0.48, 0.53, and 0.64 for PBA@HMCS-1, PBA@HMCS-2, and PBA@HMCS-3, respectively (Fig. 4d), in good accordance with the above electrochemical data (Fig. 3).

To evaluate the desalination performance of PBA@HMCS electrodes under varying conditions, we also examined how changes in cell voltage (0.6–1.2 V, in 100 mg $L^{-1}$ NaCl solution) and feedwater salt concentration (100–500 ppm NaCl, with a constant cell voltage of 1.2 V) impact their performance separately. The results are illustrated in Figs. 5 and S11 (Supplementary data). The cell voltages are obviously in positive correlation with the desalination performance of all PBA@HMCS electrodes over the range of 0.6–1.2 V (Figs. 5a and S11a–b), with a higher voltage leading to better desalination performance. The desalination capacity decreased with declining cell voltages from 1.2 to 0.6 V and instantly restored to its initial value when the cell voltage was turned back to 1.2 V. This enhancement in desalination performance at higher voltages can be attributed to the combination of improved EDL capacitance of the carbon-based HMCSs and enhanced Faradaic capacitance of NiHCF components [54,62].

It is worth noting that although the SAC increases with increasing cell voltage, the cell voltages applied in CDI are generally below the critical value for water decomposition (1.23 V) [63]. Therefore, the impact of the feedwater salt concentration on the electrode's desalination performance was further analyzed at a cell voltage of 1.2 V. It is evident that higher salt concentrations lead to an increase in adsorption and desorption rates during a charge-discharge cycle, thereby facilitating these processes to reach a state of equilibrium (Fig. 5b and S11c–d). The dependence of SACs on feedwater salt concentrations (Fig. 5c) reveals that the PBA@HMCS electrode shows a higher SAC when exposed to elevated salt concentrations due to the cumulative effects at higher NaCl concentrations [64]. For instance, the SAC of the PBA@HMCS-3 electrode in a 500 mg $L^{-1}$ NaCl solution reached up to 80.5 mg $g^{-1}$, which further decreased gradually to 74.1 and 44.5 mg $g^{-1}$ with reducing feedwater salt concentrations from 200 to 100 mg $L^{-1}$, respectively. Similar trends were observed for the other electrodes, implying the same mechanism of salt capturing. Notably, in terms of the SAC alone, the PBA@HMCS-3 electrode can be sorted as one of the best electrodes among numerous PBA/C composite electrodes with similar components (Table 1) [12,30,31,33–36,58,65]. Its SACs at 1.2 V in NaCl solutions (100–500 mg $L^{-1}$) surpassed most of the PBA-based electrodes under the same conditions (Fig. 5d) [66–69]. The remarkable desalination capacity and efficiency of PBA@HMCS-3 are likely attributed to the synergistic effect of NiHCF and HMCS-3. The highly conductive HMCS within PBA@HMCS-3 provides additional ion-accessible surfaces and active sites for NiHCF, preventing particle agglomeration and facilitating efficient charge transfer and ionic diffusion during desalination processes, thereby ensuring enhanced accessibility and mobility of $Na^+$ ions. This also suggests that optimizing the integration of NiHCF and HMCS-3 to form a rational hierarchical structure is a promising strategy for improving the desalination performance of the resulting composite electrodes.

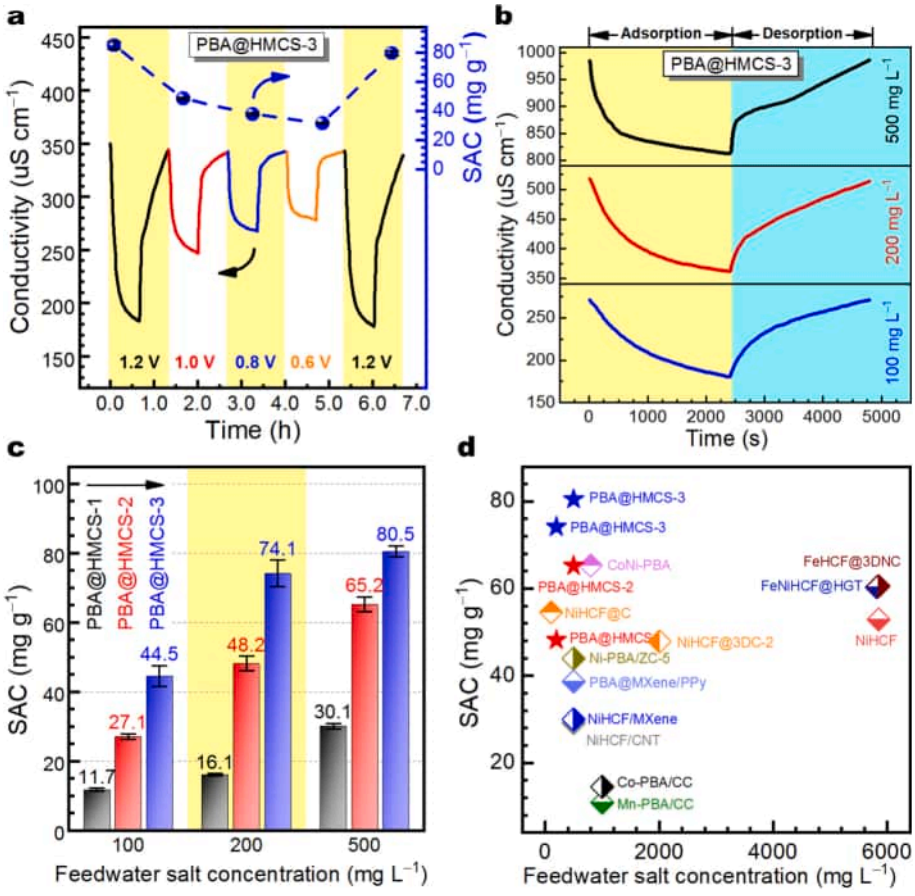


**Fig. 5.** (**a**) Plots of conductivity versus time of PBA@HMCS-3 electrode in 100 mg $L^{-1}$ NaCl solution at different cell voltages (solid line) and plots of SACs versus cell voltage (symbol with dash-line); (**b**) plot of conductivity versus time for PBA@HMCS-3 electrode at 1.2 V in feedwater of different salt concentrations; (**c**) plot of SACs versus feedwater salt concentration for PBA@HMCS electrode; (**d**) comparison in SACs of PBA-based electrodes applied in CDI (note: details of each electrode label and reference can be found in Table 1).

**Table 1**
Comparison of salt adsorption capacity of PBA-based electrodes applied to CDI.

| Electrode pair[a] | Feed salinity (mg $L^{-1}$) | Cell voltage (V) | Cell mode[c] | SAC (mg $g^{-1}$) | Ref. |
|---|---|---|---|---|---|
| NiHCF@C[b] | 100 | 1.2 | RCDI | 54.6 | [12] |
| AC//NiHCF@3 DC-2 | 20,000 | 1.2 | HCDI | 47.8 | [30] |
| Co-PBA/CC[b] | 1000 | 1.0 | CDI | 14.5 | [31] |
| AC//Ni-PBA/ZC-5 | 500 | 1.2 | HCDI | 43.9 | [33] |
| FeNiHCF@HGT[b] | 5844 | 1.2 | CDI | 60.2 | [34] |
| FeHCF/CNT[b] | 5844 | 1.0 | RCDI | 103.4 | [35] |
| AC//NiHCF/ MXene | 500 | 1.2 | HCDI | 30.0 | [36] |
| AC//NiHCF/CNT | 500 | 1.2 | HCDI | 29.1 | [58] |
| AgCl//NiHCF | 5844 | 1.2 | RCDI | 52.9 | [66] |
| AC// PBA@MXene/ PPy | 500 | 1.2 | HCDI | 38.7 | [68] |
| CC//Mn-PBA/CC | 1000 | 1.0 | HCDI | 10.9 | [67] |
| AC//CoNi-PBA | 800 | 1.2 | HCDI | 65.3 | [69] |
| FeHCF@3DNC[b] | 5844 | 1.0 | RCDI | 60.5 | [65] |
| PBA@HMCS-3[b] | 100 | 1.2 | RCDI | 44.5 | This study |
| PBA@HMCS-3[b] | 200 | 1.2 | RCDI | 74.1 | This study |
| PBA@HMCS-3[b] | 500 | 1.2 | RCDI | 80.5 | This study |

[a] NiHCF@C: NiHCF coated by carbon; AC//NiHCF@3 DC-2: AC as the anode while NiHCF loaded 3D carbon nanosheet networks (3 DC) as cathode; Co-PBA/CC: Co-PBA loaded carbon cloth (CC); FeNiHCF@HGT: FeNiHCF loaded hollow graphite tube (HGT); FeHCF/CNT: FeHCF loaded CNT; AC//NiHCF/MXene: AC as the anode while NiHCF loaded $Ti_3C_2T_x$ (MXene) as cathode; AC//NiHCF/CNT: AC as the anode while NiHCF loaded CNT as cathode; AC//PBA@MXene/PPy: AC as the anode while Ni/*Co*-PBA loaded MXene and polypyrrole (PPy) as cathode; CC//Mn-PBA/CC: carbon cloth (CC) as the anode while Mn-PBA loaded CC as cathode; FeHCF@3DNC: FeHCF loaded 3D nitrogen-doped carbon framework (3DNC); PBA@HMCS-3: NiHCF integrated with hollow mesoporous carbon sphere (HMCS).
[b] Symmetric electrode pair.
[c] CDI: capacitive deionization; HCDI: hybrid capacitive deionization; RCDI: rocking-chair capacitive deionization.

### 3.4. Cycling performance

The durability of electrodes over repeated cycles plays a crucial role in shaping the potential applications of materials. To examine the long-term stability of the PBA@HMCS electrodes applied in CDI, a consecutive charge-discharge cycling test was initially performed over 60 runs at 1.2 V in a 500 mg $L^{-1}$ NaCl solution. The feedwater conductivity and the relevant SAC profiles are depicted in Fig. S12. Both conductivity and SAC decrease with the number of cycles, consistent with previous reports on PBA-based composite electrodes [28,33,35,36,65,69]. This degradation is indicative of the deterioration of the PBA@HMCS electrodes during charge-discharge cycling [12,70]. Specifically, the PBA@HMCS-1 electrode exhibited a linear decline in SAC, from 39.6 to 9.79 mg $g^{-1}$, corresponding to a SAC retention of 24.7 % (Fig. 6a). In contrast, PBA@HMCS-2 and PBA@HMCS-3 electrodes demonstrated a two-stage linear descent in SAC (Fig. S12d). PBA@HMCS-3 underwent a rapid SAC drop during the initial 0–24 cycles, followed by a slow decline at a rate similar to that of PBA@HMCS-1, while PBA@HMCS-2 experienced a rapid descent from 0 to 28 cycles before a gentle decrease at the same rate, leading to SAC retentions of 26.2 % and 27.4 % for PBA@HMCS-2 and PBA@HMCS-3, respectively (Fig. 6a). Recall that PBA@HMCS-1 is featured by a mixed yolk-shell and core-shell structure (Fig. 2d), whereas the other two PBA@HMCS are composed of yolk-shell structured PBA@HMCS micropellets and unwrapped PBA particulates (Fig. 2e–f). To identify whether the PBA or the HMCS constituent contributed mainly to the recession of the SAC, we examined the cycling performance of PBA and PBA@HMCS electrodes at 0.8 V in 500 mg $L^{-1}$ NaCl solution and measured the concentrations of leachable $Fe^{3+}$ in the feed solutions after 60 runs (Figs. 6b, S13–14). Interestingly, the cycling stability of all PBA@HMCS electrodes has been improved at 0.8 V compared to that at 1.2 V due to the less trend of electrochemical oxidation of both the carbon and the PBA constituent as a lower voltage [71–73]. Note that the PBA@HMCS electrodes experienced significant loss after consecutive cycling for 60 cycles, with 10.5–12.2 wt% of iron being dissolved during the cycling (Fig. S14). This finding is further confirmed by the corresponding XRD and XRF results with substantial phase and chemical composition losses of the PBA component after cycling (Fig. 6c–d). In contrast, HMCSs synthesized at high temperatures (> 600 °C) usually exhibit remarkable resistance to oxidation due to the enhanced graphitic structure and unique hollow architecture [74]. Collectively, it is rational to ascribe the recession in SACs to the structural degradation and dissolution of PBA particulates over time during the cycling test.

The results of the cycling test at 0.8 V reveal that the cycling stability follows the order PBA@HMCS-3 > PBA > PBA@HMCS-2 > PBA@HMCS-1 (Fig. 6b), demonstrating the protective role of the HMCS-3 shell layer in the case of PBA@HMCS-3. Recall that the HMCS-3 has the smallest mesopore channel among all three HMCSs, showing the highest cycling stability compared to the other two PBA@HMCS electrodes. Furthermore, the yolk-shell PBA@HMCS structures provide more voids for ion storage compared to core-shell structures [20], resulting in SACs decreasing in the order: PBA@HMCS-3 > PBA@HMCS-2 > PBA@HMCS-1 (Figs. 6b and S14d). Therefore, further regulation of the TPOS:TEOS ratio and thereof the mesopore channels of the resulting HCMS should be explored in the follow-up studies for leveraging the advantage of such yolk-shell PBA@HMCS in CDI applications. Collectively, these results highlight the trade-off between SAC and cycling durability in PBA-based composite electrodes. Although the PBA@HMCS electrodes did not surpass other PBA-carbon composites in cycling performance [28,33,35,36,65,69], the findings underscore the potential of hierarchical yolk-shell PBA@HMCS composites with tunable structures as a promising direction for future CDI electrode design, though further exploration is needed to fully leverage their stability with improved conductivity.

### 3.5. Selectivity

Exploring ion selectivity in solutions of environmentally relevant compositions or real brines is vital from a practical perspective [75]. The ion selectivity properties of PBA@HMCS electrodes were investigated in a synthetic brine with multicomponent ratio same as the brine from the East Taijinaier Salt Lake ($Li^+$:$Na^+$:$K^+$:$Mg^{2+}$:$Ca^{2+}$ = 4:79:16:18:5). As shown in Fig. 6e, the concentration change ($\Delta \boldsymbol{c}$) of all ions increased over time during a single charge run of the PBA@HMCS-3 electrode, with $\Delta \boldsymbol{c}(Na^+)$ exhibiting a significantly broader range (2–18 mM) compared to the other ions (0.3–3 mM). This variation in concentration changes indicates differences in the insertion behavior of the ions over the PBA@HMCS-3 electrode. Using an equation similar to Eq. 2, we calculated the corresponding ion adsorption capacities ($\boldsymbol{\Gamma}$) for each ion. Notably, compared to other ions such as $Li^+$, $Ca^{2+}$, $Mg^{2+}$, and $K^+$ (Fig. S15), all PBA@HMCS electrodes showed a high affinity for $Na^+$ ions, as evident from their ion adsorption capacities ($\boldsymbol{\Gamma}$): PBA@HMCS-3 (12.6 mmol $g^{-1}$), PBA@HMCS-2 (14.96 mmol $g^{-1}$), and PBA@HMCS-1 (10.23 mmol $g^{-1}$). One probable reason for this phenomenon appears to be the high concentration gradient and thus the cumulative effect resulting from the much higher concentration of $Na^+$ in the synthetic brine [64].

Unlike NiHCF-based electrodes, which typically favor monovalent ions over divalent ions [12,76], the PBA@HMCS electrodes showed varying ion preferences, potentially due to their distinct yolk-shell structures and the ion sieve effect of mesoporous channels of the carbon shell [74]. To better understand the specific ion preferences of each PBA@HMCS electrode, we calculated the separation factors ($\boldsymbol{\beta}$) using the

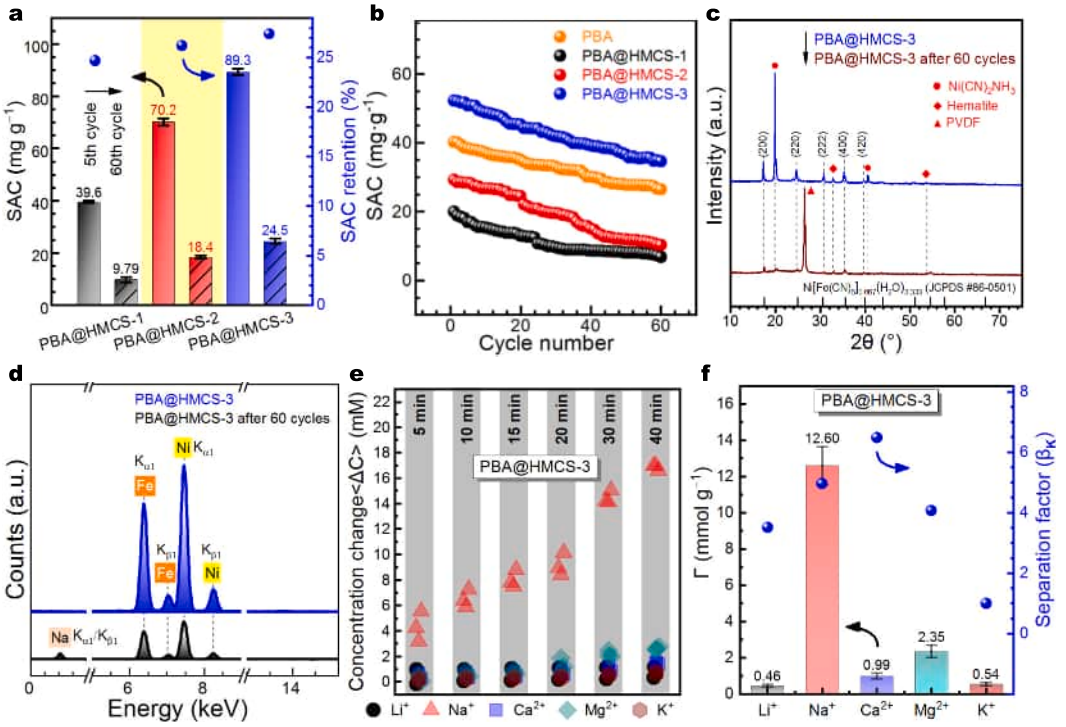


**Fig. 6.** (**a**) Comparison of SACs of the 5th and 60th cycle and the corresponding SAC retention of PBA@HMCS electrodes; (**b**) cycling stability of PBA@HMCS electrodes in 500 mg $L^{-1}$ NaCl solution at 0.8 V; (**c**) XRD patterns and (**d**) XRF spectra of PBA@HMCS-3 electrode before and after 60-cycle of consecutive charge-discharge operations, the decreases in XRD reflections and XRF peaks indicate the structural and componential degeneration of the electrode; (**e**) plots of concentration change ($\Delta c$, mM) of different cations versus time in simulated brine applied in RCDI with PBA@HMCS-3 electrode, and (**f**) the corresponding ion adsorption capacity ($\Gamma$, mmol $g^{-1}$) and separation factors to $K^+$ ($\beta_K$).

minimal $\Delta c/c$ as a reference (Eq. 4). Notably, the PBA@HMCS-3 electrode exhibited impressive selectivity, with separation factors of 3.5, 5.0, 6.5, and 4.1 for $Li^+$, $Na^+$, $Ca^{2+}$, and $Mg^{2+}$, respectively, over $K^+$. In contrast, PBA@HMCS-1 and PBA@HMCS-2 demonstrated relatively lower separation factors to the minimum $\Delta c/c$ separately, ranging from 1 to 2.5 (Fig. S15c–d).

Interestingly, the separation factors of PBA@HMCS-3 deviated from the expected trend based on ionic radii ($r$, $r_{Mg} < r_{Li} < r_{Ca} < r_{Na}$), where $\beta_{Ca/K}$ and $\beta_{Mg/K}$ would be expected to and do exceed $\beta_{Na/K}$ and $\beta_{Li/K}$, respectively (i.e., $\beta_{Ca/K} > \beta_{Na/K}$, $\beta_{Mg/K} > \beta_{Li/K}$, Fig. 6f), since smaller hydrated ions are more likely to be selectively removed over larger hydrated ions [77]. However, the separation factor of $Na^+$ over $K^+$ ($\beta_{Na/K}$) was slightly higher than that of $Mg^{2+}$ over $K^+$ ($\beta_{Mg/K}$), contrary to the above trend of ionic radii, which is likely attributed to the high concentration of $Na^+$ in the synthetic brine that brings about the cumulative effect, influencing the selectivity of PBA@HMCS-3 toward different ions. Besides, the complex architecture of PBA@HMCS-3, comprising yolk-shell PBA@HMCS, unwrapped PBA, and unloaded HMCS (Fig. 2), likely plays a significant role in determining its ion selectivity. Collectively, this unnatural preferential behavior may be attributed to the structural differences among the PBA@HMCS electrodes and the complex interplay of ionic radii and concentration gradients in the synthetic brine. Further studies are needed to clarify the role of the different components within the PBA@HMCS-3 architecture in determining its ion selectivity. Nevertheless, the PBA@HMCS-3 electrode is very promising for selective separation of specific ions (e.g., $Ca^{2+}$, $Na^+$, $Mg^{2+}$, and $Li^+$) from dicationic brines with $K^+$ due to its high repulsion against $K^+$ ions.

## 4. Conclusions

In conclusion, we successfully developed a high-performance PBA@HMCS nanocomposite electrode tailored for capacitive deionization (CDI) by optimizing the integration of nickel hexacyanoferrate (NiHCF) with hollow mesoporous carbon spheres (HMCS). Despite the high theoretical ion storage capacity of NiHCF, its application in CDI has been limited by structural flaws and poor conductivity. By strategically encapsulating NiHCF within HMCS, we created the PBA@HMCS nanocomposite electrodes that have demonstrated exceptional electrochemical desalination performance, with PBA@HMCS-3 achieving a maximum salt adsorption capacity of 80.5 mg $g^{-1}$ in a 500 mg $L^{-1}$ NaCl solution at 1.2 V. The PBA@HMCS electrodes exhibited remarkable versatility in CDI across a range of voltages and initial concentrations, highlighting their efficiency in diverse scenarios. Additionally, our ion selectivity results indicate that the PBA@HMCS-3 electrode has a high repulsion against $K^+$, highlighting its potential for selectively separating specific ions from dicationic brines with $K^+$ ions. These findings collectively underscore the vast potential of hierarchical yolk-shell PBA@HMCS as a promising choice for future CDI electrode design, and highlight the need for more hierarchically structural design of composite electrodes for high-performance CDI systems.

## Declaration of competing interest

The authors declare that they have no known competing financial interests or personal relationships that could have appeared to influence the work reported in this paper.

## Acknowledgments

The authors are grateful to Dr. Jun Li and Dr. Mingzhe Dong at the Qinghai Institute of Salt Lakes, Chinese Academy of Sciences for providing the East Taijinaier Salt Lake brine.

## Appendix A. Supplementary data

Supplementary data to this article can be found online at https://doi.org/10.1016/j.desal.2025.118679.

## Data availability statements

The authors declare that the data supporting the findings of this study are available within the paper and its Supplementary Information files. Should any raw data files be needed in another format they are available from the corresponding author upon reasonable request.

## References


[1] J. Eliasson, The rising pressure of global water shortages, Nature 517 (2015) 6, https://doi.org/10.1038/517006a.

[2] Y. Zhang, H. Zheng, X. Zhang, L.R. Leung, C. Liu, C. Zheng, Y. Guo, F.H.S. Chiew, D. Post, D. Kong, H.E. Beck, C. Li, G. Blöschl, Future global streamflow declines are probably more severe than previously estimated, Nat. Water 1 (2023) 261–271, https://doi.org/10.1038/s44221-023-00030-7.

[3] M.A. Alkhadra, X. Su, M.E. Suss, H.H. Tian, E.N. Guyes, A.N. Shocron, K. M. Conforti, J.P. De Souza, N. Kim, M. Tedesco, K. Khoiruddin, I.G. Wenten, J. G. Santiago, T.A. Hatton, M.Z. Bazant, Electrochemical methods for water purification, ion separations, and energy conversion, Chem. Rev. 122 (2022) 13547–13635, https://doi.org/10.1021/acs.chemrev.1c00396.

[4] M.A. Shannon, P.W. Bohn, M. Elimelech, J.G. Georgiadis, B.J. Marinas, A. M. Mayes, Science and technology for water purification in the coming decades, Nature 452 (2008) 301–310, https://doi.org/10.1038/nature06599.

[5] M. Elimelech, W.A. Phillip, The future of seawater desalination: energy, technology, and the environment, Science 333 (2011) 712–717, https://doi.org/10.1126/science.1200488.

[6] Y. Oren, Capacitive deionization (CDI) for desalination and water treatment - past, present and future (a review), Desalination 228 (2008) 10–29, https://doi.org/10.1016/j.desal.2007.08.005.

[7] M.A. Anderson, A.L. Cudero, J. Palma, Capacitive deionization as an electrochemical means of saving energy and delivering clean water. Comparison to present desalination practices: will it compete? Electrochim. Acta 55 (2010) 3845–3856, https://doi.org/10.1016/j.electacta.2010.02.012.

[8] M.E. Suss, S. Porada, X. Sun, P.M. Biesheuvel, J. Yoon, V. Presser, Water desalination via capacitive deionization: what is it and what can we expect from it? Energy Environ. Sci. 8 (2015) 2296–2319, https://doi.org/10.1039/c5ee00519a.

[9] K. Singh, S. Porada, H.D. de Gier, P.M. Biesheuvel, L.C.P.M. de Smet, Timeline on the application of intercalation materials in capacitive deionization, Desalination 455 (2019) 115–134, https://doi.org/10.1016/j.desal.2018.12.015.

[10] P. Srimuk, X. Su, J. Yoon, D. Aurbach, V. Presser, Charge-transfer materials for electrochemical water desalination, ion separation and the recovery of elements, Nat. Rev. Mater. 5 (2020) 517–538, https://doi.org/10.1038/s41578-020-0193-1.

[11] Y. Bao, J. Jin, M.Y. Ma, M. Li, F.H. Li, Ion exchange conversion of Na-Birnessite to Mg-Buserite for enhanced and preferential $Cu^{2+}$ removal via hybrid capacitive deionization, ACS Appl. Mater. Interfaces 14 (2022) 46646–46656, https://doi.org/10.1021/acsami.2c13086.

[12] Y. Bao, J.X. Hao, S. Zhang, D.C. Zhu, F.H. Li, Structural/compositional-tailoring of nickel Hexacyanoferrate electrodes for highly efficient capacitive deionization, Small 19 (2023) 2300384, https://doi.org/10.1002/smll.202300384.

[13] Z. Wang, T.T. Yan, J.H. Fang, L.Y. Shi, D.S. Zhang, Nitrogen-doped porous carbon derived from a bimetallic metal-organic framework as highly efficient electrodes for flow-through deionization capacitors, J. Mater. Chem. A 4 (2016) 10858–10868, https://doi.org/10.1039/c6ta02420c.

[14] M. Ding, W.H. Shi, L. Guo, Z.Y. Leong, A. Baji, H.Y. Yang, Bimetallic metal-organic framework derived porous carbon nanostructures for high performance membrane capacitive desalination, J. Mater. Chem. A 5 (2017) 6113–6121, https://doi.org/10.1039/c7ta00339k.

[15] J.B. Lee, K.K. Park, S.W. Yoon, P.Y. Park, K.I. Park, C.W. Lee, Desalination performance of a carbon-based composite electrode, Desalination 237 (2009) 155–161, https://doi.org/10.1016/j.desal.2007.11.058.

[16] Y.J. Kim, J.H. Choi, Selective removal of nitrate ion using a novel composite carbon electrode in capacitive deionization, Water Res. 46 (2012) 6033–6039, https://doi.org/10.1016/j.watres.2012.08.031.

[17] L.K. Pan, X.Z. Wang, Y. Gao, Y.P. Zhang, Y.W. Chen, Z. Sun, Electrosorption of anions with carbon nanotube and nanofibre composite film electrodes, Desalination 244 (2009) 139–143, https://doi.org/10.1016/j.desal.2008.05.019.

[18] P.Y. Liu, T.T. Yan, L.Y. Shi, H.S. Park, X.C. Chen, Z.G. Zhao, D.S. Zhang, Graphene-based materials for capacitive deionization, J. Mater. Chem. A 5 (2017) 13907–13943, https://doi.org/10.1039/c7ta02653f.

[19] M. Al Radi, E.T. Sayed, H. Alawadhi, M.A. Abdelkareem, Progress in energy recovery and graphene usage in capacitive deionization, Crit. Rev. Environ. Sci. Technol. 52 (2022) 3080–3136, https://doi.org/10.1080/10643389.2021.1902698.

[20] X.H. Liu, X.T. Xu, X.X. Xuan, W. Xia, G.L. Feng, S.H. Zhang, Z.G. Wu, B.H. Zhong, X.D. Guo, K.Y. Xie, Y. Yamauchi, Unlocking enhanced capacitive deionization of $NaTi_2(PO_4)_3$/carbon materials by the yolk-Shell design, J. Am. Chem. Soc. 145 (2023) 9242–9253, https://doi.org/10.1021/jacs.3c01755.

[21] Z.W. Hao, X.Q. Sun, J.B. Chen, X.F. Zhou, Y.L. Zhang, Recent Progress and challenges in faradic capacitive desalination: from mechanism to performance, Small 19 (2023) 2300253, https://doi.org/10.1002/smll.202300253.

[22] M.E. Suss, V. Presser, Water desalination with energy storage electrode materials, Joule 2 (2018) 10–15, https://doi.org/10.1016/j.joule.2017.12.010.

[23] W.J. Li, C. Han, G. Cheng, S.L. Chou, H.K. Liu, S.X. Dou, Chemical properties, structural properties, and energy storage applications of Prussian blue analogues, Small 15 (2019) 1900470, https://doi.org/10.1002/smll.201900470.

[24] C.D. Wessells, S.V. Peddada, R.A. Huggins, Y. Cui, Nickel Hexacyanoferrate nanoparticle electrodes for aqueous sodium and potassium ion batteries, Nano Lett. 11 (2011) 5421–5425, https://doi.org/10.1021/nl203193q.

[25] J. Lee, S. Kim, J. Yoon, Rocking chair desalination battery based on Prussian blue electrodes, ACS Omega 2 (2017) 1653–1659, https://doi.org/10.1021/acsomega.6b00526.

[26] S. Porada, A. Shrivastava, P. Bukowska, P.M. Biesheuvel, K.C. Smith, Nickel Hexacyanoferrate electrodes for continuous cation intercalation desalination of brackish water, Electrochim. Acta 255 (2017) 369–378, https://doi.org/10.1016/j.electacta.2017.09.137.

[27] C.L. Li, Y.C. Xiong, X.J. Shen, D. Luo, W.J. Wu, Z.T. Li, M.H. Helal, Z.M. El-Bahy, Y. Y. Mai, Z. Liu, Y. Yamauchi, X.T. Xu, Fundamental understanding of Prussian blue and its analogues for superior capacitive deionization: a perspective from nanoarchitectonics, Coord. Chem. Rev. 520 (2024) 216100, https://doi.org/10.1016/j.ccr.2024.216100.

[28] Z.B. Ding, X.T. Xu, Y.Q. Li, K. Wang, T. Lu, L.K. Pan, Significantly improved stability of hybrid capacitive deionization using nickel hexacyanoferrate/reduced graphene oxide cathode at low voltage operation, Desalination 468 (2019) 114078, https://doi.org/10.1016/j.desal.2019.114078.

[29] S. Vafakhah, L. Guo, D. Sriramulu, S.Z. Huang, M. Saeedikhani, H.Y. Yang, Efficient sodium-ion intercalation into the freestanding Prussian blue/graphene aerogel anode in a hybrid capacitive deionization system, ACS Appl. Mater. Interfaces 11 (2019) 5989–5998, https://doi.org/10.1021/acsami.8b18746.

[30] S.Y. Wang, G. Wang, Y.W. Wang, H.R. Song, S.H. Lv, T.Z. Li, C.P. Li, In situ formation of Prussian blue analogue nanoparticles decorated with three-dimensional carbon Nanosheet networks for superior hybrid capacitive deionization performance, ACS Appl. Mater. Interfaces 12 (2020) 44049–44057, https://doi.org/10.1021/acsami.0c12421.

[31] X.Y. Zhang, J. Dutta, X-Fe (X = Mn, Co, Cu) Prussian blue analogue-modified carbon cloth electrodes for capacitive deionization, ACS Appl. Energy Mater. 4 (2021) 8275–8284, https://doi.org/10.1021/acsaem.1c01501.

[32] D.V. Cuong, C.H. Hou, Nickel hexacyanoferrate incorporated with reduced graphene oxide for highly efficient intercalation desalination, Sep. Purif. Technol. 295 (2022) 121351, https://doi.org/10.1016/j.seppur.2022.121351.

[33] F.Y. Meng, Z.B. Ding, X.T. Xu, Y. Liu, T. Lu, L.K. Pan, Metal organic framework-derived nitrogen-doped porous carbon sustained Prussian blue analogues for efficient and fast hybrid capacitive deionization, Sep. Purif. Technol. 317 (2023) 123899, https://doi.org/10.1016/j.seppur.2023.123899.

[34] Z.Y. Tang, B. Hu, P.F. Nie, X.H. Shang, J.M. Yang, J.Y. Liu, Bimetallic Fe, Ni-PBA on hollow graphite tube for capacitive deionization with exceptional stability, Chem. Eng. J. 466 (2023) 143216, https://doi.org/10.1016/j.cej.2023.143216.

[35] A.O. Gong, Y.B. Zhao, B.L. Liang, K.X. Li, Stepwise hollow Prussian blue/carbon nanotubes composite as a novel electrode material for high-performance desalination, J. Colloid Interface Sci. 605 (2022) 432–440, https://doi.org/10.1016/j.jcis.2021.07.103.

[36] Z.Q. Chen, Z.B. Ding, Y.Y. Chen, X.T. Xu, Y. Liu, T. Lu, L.K. Pan, Three-dimensional charge transfer pathway in close-packed nickel hexacyanoferrate-on-MXene nano-stacking for high-performance capacitive deionization, Chem. Eng. J. 452 (2023) 139451, https://doi.org/10.1016/j.cej.2022.139451.

[37] A.A. Obisanya, L. Ma, J.K. Liu, T.S. Yang, Z.B. Ren, X.Y. Tan, F.M. Gao, J.R. Wang, Multiscale scrutinizing ion storage kinetics in hollow Ni-Mn Prussian blue analogues for enhanced capacitive deionization, Adv. Funct. Mater. 34 (2024) 2404591, https://doi.org/10.1002/adfm.202404591.

[38] J.N. Zheng, S.L. Ju, G.L. Xia, H.G. Pan, X.B. Yu, Co-construction of solid solution phase and void space in yolk-Shell $Fe_{0.4}Co_{0.6}S$@N-doped carbon to enhance cycling capacity and rate capability for aluminum-ion batteries, ACS Appl. Mater. Interfaces 14 (2022) 8076–8085, https://doi.org/10.1021/acsami.1c24510.

[39] H. Wang, T.T. Yan, L.Y. Shi, G.R. Chen, J.P. Zhang, D.S. Zhang, Creating nitrogen-doped hollow multiyolk@Shell carbon as high performance electrodes for flow-through deionization capacitors, ACS Sustain. Chem. Eng. 5 (2017) 3329–3338, https://doi.org/10.1021/acssuschemeng.6b03183.

[40] Y. Tang, S. Cao, W. Feng, X. Guo, Y. Sun, S. Zhang, H. Xue, H. Pang, Spatial confinement effect on hollow mesoporous carbon spheres/MOF-derived nanosheets superstructures for improved capacitive deionization performance, Nano Res. 18 (2025) 94907194, https://doi.org/10.26599/NR.2025.94907194.

[41] D.P. Domonov, S.I. Pechenyuk, Y.P. Semushina, Thermal decomposition of Prussian blue analogues in various gaseous media, J. Therm. Anal. Calorim. 146 (2021) 629–635, https://doi.org/10.1007/s10973-020-09936-w.

[42] H.W. Zhang, O. Noonan, X.D. Huang, Y.N. Yang, C. Xu, L. Zhou, C.Z. Yu, Surfactant-free assembly of mesoporous carbon hollow spheres with large tunable pore sizes, ACS Nano 10 (2016) 4579–4586, https://doi.org/10.1021/acsnano.6b00723.

[43] X.K. Wan, H.B. Wu, B.Y. Guan, D.Y. Luan, X.W. Lou, Confining sub-nanometer Pt clusters in hollow mesoporous carbon spheres for boosting hydrogen evolution activity, Adv. Mater. 32 (2020) 1901349, https://doi.org/10.1002/adma.201901349.

[44] R. Rehman, J. Peng, H.C. Yi, Y. Shen, J.W. Yin, C. Li, C. Fang, Q. Li, J.T. Han, Highly crystalline nickel hexacyanoferrate as a long-life cathode material for

sodium-ion batteries, RSC Adv. 10 (2020) 27033–27041, https://doi.org/10.1039/d0ra03490h.
[45] Z.Y. Wu, M. Karamad, X. Yong, Q.Z. Huang, D.A. Cullen, P. Zhu, C.A. Xia, Q. F. Xiao, M. Shakouri, F.Y. Chen, J.Y. Kim, Y. Xia, K. Heck, Y.F. Hu, M.S. Wong, Q. L. Li, I. Gates, S. Siahrostami, H.T. Wang, Electrochemical ammonia synthesis via nitrate reduction on Fe single atom catalyst, Nat. Commun. 12 (2021) 2870, https://doi.org/10.1038/s41467-021-23115-x.
[46] K. Singh, G. Li, J. Lee, H. Zuilhof, B.L. Mehdi, R.L. Zornitta, L.C.P.M. de Smet, Divalent ion selectivity in capacitive deionization with vanadium hexacyanoferrate: experiments and quantum-chemical computations, Adv. Funct. Mater. 31 (2021) 215203, https://doi.org/10.1002/adfm.202105203.
[47] S.Y. Wang, Y.H. Lei, C.P. Li, L. Zhao, S.W. Du, G. Wang, J.S. Qiu, Enabling high capacity and stable sodium capture in simulated saltwater by highly crystalline Prussian blue analogues cathode, Small Struct. 5 (2024) 2400163, https://doi.org/10.1002/sstr.202400163.
[48] M. Ezzati, F. Hekmat, S. Shahrokhian, H.E. Unalan, Titanium disulfide decorated hollow carbon spheres towards capacitive deionization, Desalination 533 (2022) 115766, https://doi.org/10.1016/j.desal.2022.115766.
[49] B. Feng, Z.U. Khan, W.U. Khan, 3D graphene-supported N-doped hierarchically porous carbon for capacitive deionization of saline water, Environ. Sci.- Nano 10 (2023) 1163–1176, https://doi.org/10.1039/d2en01103d.
[50] F.H. Li, J.J. Fu, J. Jin, S.L. Wang, Y.Y. Liu, M. Yang, X.R. Fu, Evaporation-induced self-assembly (EISA) synthesized mesoporous bimetallic oxides (MBOs) enabling enhanced co-uptake of arsenate and fluoride from water, J. Chem. Technol. Biotechnol. 94 (2019) 879–891, https://doi.org/10.1002/jctb.5835.
[51] J. Wang, J. Polleux, J. Lim, B. Dunn, Pseudocapacitive contributions to electrochemical energy storage in TiO2(anatase) nanoparticles, J. Phys. Chem. C 111 (2007) 14925–14931, https://doi.org/10.1021/jp074464w.
[52] N. Elgrishi, K.J. Rountree, B.D. McCarthy, E.S. Rountree, T.T. Eisenhart, J. L. Dempsey, A practical Beginner's guide to cyclic voltammetry, J. Chem. Educ. 95 (2018) 197–206, https://doi.org/10.1021/acs.jchemed.7b00361.
[53] K.J. Tan, X. Su, T.A. Hatton, An asymmetric Iron-based redox-active system for electrochemical separation of ions in aqueous media, Adv. Funct. Mater. 30 (2020) 1910363, https://doi.org/10.1002/adfm.201910363.
[54] T. Brezesinski, J. Wang, S.H. Tolbert, B. Dunn, Ordered mesoporous α-$MoO_3$ with iso-oriented nanocrystalline walls for thin-film pseudocapacitors, Nat. Mater. 9 (2010) 146–151, https://doi.org/10.1038/Nmat2612.
[55] M. Zhang, Y.F. Tong, Z.P. Sun, J.W. Wang, Y.L. Lin, F.Y. Kang, Q.C. Zhang, W. W. Huang, Two-dimensional covalent organic framework with synergistic active centers for efficient electrochemical sodium storage, Chem. Mater. 35 (2023) 4873–4881, https://doi.org/10.1021/acs.chemmater.3c00983.
[56] D.L. Chao, C.R. Zhu, P.H. Yang, X.H. Xia, J.L. Liu, J. Wang, X.F. Fan, S.V. Savilov, J. Y. Lin, H.J. Fan, Z.X. Shen, Array of nanosheets render ultrafast and high-capacity Na-ion storage by tunable pseudocapacitance, Nat. Commun. 7 (2016) 12122, https://doi.org/10.1038/ncomms12122.
[57] J. Jin, M. Li, M.T. Tang, Y. Li, Y.Y. Liu, H. Cao, F.H. Li, Phase- and crystallinity-tailorable $MnO_2$ as an electrode for highly efficient hybrid capacitive deionization (HCDI), ACS Sustain. Chem. Eng. 8 (2020) 11424–11434, https://doi.org/10.1021/acssuschemeng.0c04101.
[58] L.M. Xu, Z.B. Ding, Y.Y. Chen, X.T. Xu, Y. Liu, J.B. Li, T. Lu, L.K. Pan, Carbon nanotube bridged nickel hexacyanoferrate architecture for high-performance hybrid capacitive deionization, J. Colloid Interface Sci. 630 (2023) 372–381, https://doi.org/10.1016/j.jcis.2022.10.140.
[59] H. Xu, Y.F. Cao, Y. Li, P. Cao, D.D. Liu, Y.Y. Zhang, Q.W. Li, High-loading co-doped NiO nanosheets on carbon-welded carbon nanotube framework enabling rapid charge kinetic for enhanced supercapacitor performance, journal of energy, Chemistry 50 (2020) 240–247, https://doi.org/10.1016/j.jechem.2020.03.023.
[60] S. Porada, R. Zhao, A. van der Wal, V. Presser, P.M. Biesheuvel, Review on the science and technology of water desalination by capacitive deionization, Prog. Mater. Sci. 58 (2013) 1388–1442, https://doi.org/10.1016/j.pmatsci.2013.03.005.
[61] T. Kim, J. Yoon, CDI ragone plot as a functional tool to evaluate desalination performance in capacitive deionization, RSC Adv. 5 (2015) 1456–1461, https://doi.org/10.1039/c4ra11257a.
[62] W.H. Shi, X.Y. Liu, T.Q. Deng, S.Z. Huang, M. Ding, X.H. Miao, C.Z. Zhu, Y.H. Zhu, W.X. Liu, F.F. Wu, C.J. Gao, S.W. Yang, H.Y. Yang, J.N. Shen, X.H. Cao, Enabling superior sodium capture for efficient water desalination by a tubular polyaniline decorated with Prussian blue nanocrystals, Adv. Mater. 32 (2020) 1907404, https://doi.org/10.1002/adma.201907404.
[63] M.T.Z. Myint, J. Dutta, Fabrication of zinc oxide nanorods modified activated carbon cloth electrode for desalination of brackish water using capacitive deionization approach, Desalination 305 (2012) 24–30, https://doi.org/10.1016/j.desal.2012.08.010.
[64] X.J. Shen, R.T. Hai, X.H. Wang, Y. Li, Y.Y. Wang, F. Yu, J. Ma, Free-standing 3D alkalized $Ti_3C_2T_x$/$Ti_3C_2T_x$ nanosheet membrane electrode for highly efficient and stable desalination in hybrid capacitive deionization, J. Mater. Chem. A 8 (2020) 19309–19318, https://doi.org/10.1039/d0ta06994a.
[65] A. Gong, Y.B. Zhao, M.M. He, B.L. Liang, K.X. Li, High-performance desalination of three-dimensional nitrogen-doped carbon framework reinforced Prussian blue in capacitive deionization, Desalination 505 (2021) 114997, https://doi.org/10.1016/j.desal.2021.114997.
[66] J. Lee, J. Lee, J. Ahn, K. Jo, S.P. Hong, C. Kim, C. Lee, J. Yoon, Enhancement in desalination performance of battery electrodes via improved mass transport using a multichannel flow system, ACS Appl. Mater. Interfaces 11 (2019) 36580–36588, https://doi.org/10.1021/acsami.9b10003.
[67] X.Y. Zhang, E.A. Toledo-Carrillo, D.K. Yu, J. Dutta, Effect of surface charge on the fabrication of hierarchical Mn-based Prussian blue analogue for capacitive desalination, ACS Appl. Mater. Interfaces 14 (2022) 40371–40381, https://doi.org/10.1021/acsami.2c08192.
[68] Y.M. Cai, W. Zhang, J.S. Zhao, Y. Wang, Flexible structural construction of the ternary composite Ni,Co-Prussian blue analogue@MXene/polypyrrole for high-capacity capacitive deionization, Appl. Surf. Sci., 622 (2023) 156926. doi:https://doi.org/10.1016/j.apsusc.2023.156926.
[69] R.A. Liu, Y. Wang, Y.D. Wu, X. Ye, W.F. Cai, Controllable synthesis of nickel-cobalt-doped Prussian blue analogs for capacitive desalination, Electrochim. Acta 442 (2023) 141815, https://doi.org/10.1016/j.electacta.2023.141815.
[70] Y.X. Huang, M. Xie, Z.H. Wang, Y. Jiang, Y. Yao, S.J. Li, Z.H. Li, L. Li, F. Wu, R. J. Chen, A chemical precipitation method preparing hollow-Core-Shell heterostructures based on the Prussian blue analogs as cathode for sodium-ion batteries, Small 14 (2018) 1801246, https://doi.org/10.1002/smll.201801246.
[71] I. Cohen, E. Avraham, Y. Bouhadana, A. Soffer, D. Aurbach, Long term stability of capacitive de-ionization processes for water desalination: the challenge of positive electrodes corrosion, Electrochim. Acta 106 (2013) 91–100, https://doi.org/10.1016/j.electacta.2013.05.029.
[72] L. Jiang, Y. Lu, C. Zhao, L. Liu, J. Zhang, Q. Zhang, X. Shen, J. Zhao, X. Yu, H. Li, X. Huang, L. Chen, Y.-S. Hu, Building aqueous K-ion batteries for energy storage, Nat. Energy 4 (2019) 495–503, https://doi.org/10.1038/s41560-019-0388-0.
[73] P. Naskar, B. Biswas, S. Laha, A. Banerjee, Prussian blue analogues with $Na_2Ni_xCo_yMn_zFe(CN)_6$-multimetallic structures as positive and hydrogen vanadate as negative electrodes in aqueous Na-ion batteries for solar energy storage applications, Energy Adv. 3 (2024) 1401–1413, https://doi.org/10.1039/D4YA00178H.
[74] Q. Tian, L.Y. Jing, H.N. Du, Y.C. Yin, X.L. Cheng, J.X. Xu, J.Y. Chen, Z.X. Liu, J. Y. Wan, J. Liu, J.L. Yang, Mesoporous carbon spheres with programmable interiors as efficient nanoreactors for $H_2O_2$ electrosynthesis, Nat. Commun. 15 (2024) 983, https://doi.org/10.1038/s41467-024-45243-w.
[75] R. Wang, K. Yang, C. Wong, H. Aguirre-Villegas, R. Larson, F. Brushett, M.H. Qin, S. Jin, Electrochemical ammonia recovery and co-production of chemicals from manure wastewater, Nat. Sustain. 7 (2024) 179–190, https://doi.org/10.1038/s41893-023-01252-z.
[76] K. Singh, Z.X. Qian, P.M. Biesheuvel, H. Zuilhof, S. Porada, L.C.P.M. de Smet, Nickel hexacyanoferrate electrodes for high mono/divalent ion-selectivity in capacitive deionization, Desalination 481 (2020) 114346, https://doi.org/10.1016/j.desal.2020.114346.
[77] Y.W. Chen, J.F. Chen, C.H. Lin, C.H. Hou, Integrating a supercapacitor with capacitive deionization for direct energy recovery from the desalination of brackish water, Appl. Energy 252 (2019) 113417, https://doi.org/10.1016/j.apenergy.2019.113417.